

3-D Models of Embedded High-Mass Stars: Effects of a Clumpy Circumstellar Medium

R. Indebetouw^{1,4}, B. A. Whitney², K. E. Johnson^{1,5}, K. Wood³

ABSTRACT

We use 3-D radiative transfer models to show the effects of clumpy circumstellar material on the observed infrared colors of high mass stars embedded in molecular clouds. We highlight differences between 3-D clumpy and 1-D smooth models which can affect the interpretation of data. We discuss several important properties of the emergent spectral energy distribution (SED): More near-infrared light (scattered and direct from the central source) can escape than in smooth 1-D models. The near- and mid-infrared SED of the same object can vary significantly with viewing angle, depending on the clump geometry along the sightline. Even the wavelength-integrated flux can vary with angle by more than a factor of two. Objects with the same *average* circumstellar dust distribution can have very different near- and mid-IR SEDs depending on the clump geometry and the proximity of the most massive clump to the central source.

Although clumpiness can cause similar objects to have very different SEDs, there are some observable trends. Near- and mid-infrared colors are sensitive to the weighted average distance of clumps from the central source and to the magnitude of clumpy density variations (smooth-to-clumpy ratio). Far-infrared emission remains a robust measure of the total dust mass. We present simulated SEDs, colors, and images for 2MASS and *Spitzer* filters. We compare to observations of some UCH II regions and find that 3-D clumpy models fit better than smooth models. In particular, clumpy models with fractal dimensions in the range 2.3-2.8, smooth to clumpy ratios of $\lesssim 50\%$, and density distributions with shallow average radial density profiles fit the SEDs best ($\langle \rho \rangle \propto r^\alpha$, $-1.0 < \alpha < 0.0$).

¹University of Virginia, Astronomy Dept., P.O. Box 3818, Charlottesville, VA, 22903-0818

²Space Science Institute, 4750 Walnut St. Suite 205, Boulder, CO 80301

³School of Physics and Astronomy, University of St. Andrews, North Haugh, St Andrews, Fife, Scotland, KY16 9SS

⁴Spitzer Fellow

⁵Hubble Fellow

Subject headings: radiative transfer—stars: formation—stars: high mass—stars: pre-main sequence—circumstellar matter—dust, extinction

1. Introduction

The important question of how stars form is frequently investigated with infrared imaging, for both astrophysical and practical reasons. Young stellar objects (YSOs) are usually still deeply embedded in their natal molecular material. The distribution of this gas and dust (e.g. in an accretion disk) can reveal a great deal about the formation process, and this hot dust close to the star emits primarily in the near and mid-infrared (for this paper, we define near-IR $\equiv 1 < \lambda < 3\mu\text{m}$ and mid-IR $\equiv 3 < \lambda < 30\mu\text{m}$). Although the bulk of the dust mass is often at cooler temperatures, with SEDs peaking in the far-infrared ($\sim 100\mu\text{m}$), probing the warmer dust is both advantageous and potentially dangerous because the NIR/MIR SED is more sensitive to the dust distribution and geometric effects. The infrared is observationally advantageous because at shorter wavelengths, YSOs are completely invisible, and at longer wavelengths, detector technology is less mature and the spatial resolution of (typically diffraction-limited) observatories begins to suffer. Many current and recent observatories are infrared-optimized, such as ISO and ground-based telescopes with adaptive optics. Particularly exciting is the successful operation of the *Spitzer Space Telescope*, which is producing a wealth of MIR data on star formation due to its unprecedented mapping efficiency (Allen et al. 2004; Megeath et al. 2004; Reach et al. 2004; Whitney et al. 2004a). The IRAC instrument (Fazio et al. 2004) provides simultaneous $\lesssim 2''$ imaging at 3.6, 4.5, 5.8, and $8.0\mu\text{m}$, and MIPS (Rieke et al. 2004) provides $6''$ images at $24\mu\text{m}$, and longer wavelengths at lower resolution. It is critical that we understand how circumstellar dust geometry can affect our interpretation of all of this NIR/MIR data.

In a previous set of papers (Whitney et al. 2003a,b, 2004b) we showed how 2-D geometries (disks, rotationally flattened envelopes, bipolar cavities) affect the near-IR and mid-IR colors of Young Stellar Objects (YSOs) of various stellar masses and evolutionary states. Those models show that there is not always a direct correspondence of the $1-10\mu\text{m}$ colors or spectral index with evolutionary state, due to several effects such as scattered light, inclination, aperture size, and stellar temperature. There is a trend for younger sources to have redder colors, but there is substantial overlap and extreme exceptions to the trends. Separation of these populations in a color-color diagram generally requires supplemental longer ($\lambda > 20\mu\text{m}$) wavelength observations. If only $1-10\mu\text{m}$ SEDs are available, for example, in the Galactic Legacy Infrared Midplane Extraordinaire (GLIMPSE, a *Spitzer* project; Benjamin et al. 2003), model fits to the spectral energy distributions (SEDs) provide a more

promising avenue than color-color diagrams for interpreting the SEDs since they use the most information simultaneously (Robitaille et al. 2005, in prep.).

This paper focuses on UltraCompact H II regions, or the later stages of high mass (O and early B) star formation; although we have not yet explored the issue, we expect that the clumpiness of envelopes is important also in younger high-mass objects, and perhaps in somewhat lower-mass protostars as well. It is believed that the central sources of UltraCompactH II regions (UCH IIs; Churchwell et. al 2004) have probably reached the main sequence, possibly halted accretion and dispersed infalling material, but remain deeply embedded in their natal molecular cloud. These stars are so luminous that they heat up large volumes (~ 3 pc radius) and masses of dust and gas, which reprocess the stellar radiation towards longer wavelengths. Observations of high mass YSOs and UCH II regions are usually modeled using 1-D radiative transfer codes (Wolfire & Churchwell 1994; Faison et al. 1998; Hatchell et al. 2000; van der Tak et al. 2000; Beuther et al. 2002; Mueller et al. 2002). These are adequate for modeling long wavelength observations ($> 100\mu\text{m}$), but at shorter wavelengths, the inhomogeneous nature of the surrounding interstellar medium (e.g. Elmegreen & Falgarone 1996) likely has a large effect on the SED. This is demonstrated in the attempts by Faison et al. (1998) (hereafter F98) to fit the mid-IR spectroscopy of several UCH II sources with 1-D smooth models. For a given envelope mass set by the long wavelength flux, the models consistently produced too deep a $10\mu\text{m}$ silicate feature and too little short wavelength flux, even after decreasing the silicate abundances by a factor of two. Changing the radial density profile is insufficient to bring the models into agreement with the data. F98 use constant-density spheres with large inner holes and obtain a poor match. Some of the other models cited above use negative power-law density gradients to fit spatially resolved intensity profiles; such 1-D models still have difficulties fitting UCH II SEDs over a wide wavelength range (§3.2).

In §2 we describe our models. Three-dimensional nonhomogeneous models differ significantly from 1-D smooth models with the same amount of circumstellar dust. Some authors have computed SEDs in two-phase clumpy distributions (Misselt et al. 2001; Wolf et al. 1998). In an attempt to calculate as realistic models as possible, in this paper we calculate SEDs in hierarchically clumped density structures, following a procedure for calculating fractal density described by Elmegreen (1997) and Mathis, Whitney, & Wood (2002) and using a volume fractal dimension D similar to that calculated for the interstellar medium ($D = 2.3 - 2.6$; Elmegreen & Falgarone 1996). In §3.3 we describe the properties of the 3-D models in terms of synthetic observations: high-resolution images, spectral energy distributions, and photometric fluxes analyzed using color-color and color-magnitude diagrams. We discuss how the properties vary with viewing angle (§3.4), and show in detail how the SEDs of 1-D models cannot reproduce the characteristics of 3-D models (§3.6). In §4.1 we show

that despite the variations, there are some trends that allow observations to probe physical conditions. In §5 we demonstrate our findings on real data, and give conclusions in §6.

2. Model Construction

We use a Monte Carlo Radiative transfer code similar to that described in Whitney et al. (2003a) (Paper I), but using a 3-D grid and incorporating a hierarchically clumped density distribution. We use the radiative equilibrium method developed by Bjorkman & Wood (2001). The models solve for the 3-D temperature distribution, conserve flux absolutely, and accurately compute scattering and polarization using arbitrary scattering phase functions. The output radiation field is binned into 200 angular directions (10 polar intervals and 20 azimuth intervals), i.e. each model produces 200 SEDs corresponding to different viewing angles. We do not currently include emission from polycyclic aromatic hydrocarbons (PAHs) or transiently heated grains; these likely affect fluxes in the IRAC wavelength range (3–8 μ m). The only source of calculation error in our models is photon counting statistics – running more photons produces higher signal-to-noise spectra. The models produced for figures in this paper took 12–24 hours each to run (on a 2 GHz PC and code compiled with g77). Draft quality results sufficient to explore trends take \lesssim 2 hours.

We specify circumstellar dust distributions with a clumpy and smooth component, with the relative contribution ranging from zero (very clumpy with evacuated holes) to one (constant density). The clump distribution is specified using the algorithm of Elmegreen (1997) as implemented in Mathis, Whitney, & Wood (2002): N mass particles are randomly placed in a simulation grid of size L . N more particles are randomly placed, each within a distance $L/(2\Delta)$ of one of the particles in the previous round (Δ is a parameter which determines the approximate fractal dimension of the resulting distribution). This process is repeated twice more, so that N^4 particles are placed. The mass distribution is not a true fractal (self-similar on all scales), but merely hierarchically clumped (self-similar over about an order of magnitude in scale). Nevertheless, the quantity $D = \log(N)/\log(\Delta)$ is essentially the fractal dimension. The precise value of D does not dramatically affect any of our results – this will be demonstrated in §4.1.1, after discussing more universal properties of the models.

Different grain models could be used in different parts of the dust cocoon (e.g. larger grains in dense clumps), as in the young stellar objects modeled in Whitney et al. (2003b). For simplicity, we use the same grain model throughout the envelope; as described in Paper I, the grain distribution was fit to the extinction curve typical of molecular clouds with $R_V=4.3$ using a maximum entropy method similar to Kim, Martin, & Hendry (1994). We use spherical grains with dielectric functions for silicate and graphite from Laor & Draine

(1993). The dust sublimation temperature is chosen to be 1600 K.

For simplicity, all of the clumpy models shown in this paper are for a massive star, with the same amount of circumstellar dust, and the same photospheric spectrum of the central source (the appropriate Kurucz model). The results presented are general to all massive young stars, but we wish to isolate the effects of differing clumpy circumstellar distribution from the effects of different stellar masses and temperatures. The latter effect is discussed in (Whitney et al. 2003b) for 2-D circumstellar distributions, and further discussion of clumpy dust in the context of embedded protoclusters is presented in Johnson et al 2005 (submitted).

In order to provide a basis for comparison, we ran numerous models with the smooth-to-clumpy density ratio equal to one, i.e. constant-density spheres. In particular, we compare our results with the popular DUSTY code (Ivezic & Elitzur 1997) in Figure 1. Across a range of parameters, the SEDs are generally indistinguishable between the two codes, and quantitatively agree to a few percent. Our code properly calculates nonisotropic scattering (Paper 1), whereas DUSTY uses an isotropic scattering function. For models with low ($\tau_V \lesssim 30$) optical depth, this can increase the differences between the two codes to 10-15%, but if we run our code with isotropic scattering the results are then indistinguishable. We will demonstrate that differences between 1-D and 3-D models are far greater than any of these subtle (few percent) effects.

3. Results of a Canonical Clumpy Model

3.1. Density and Temperature Distributions

Figure 2 shows an azimuthal slice through the density grid of our canonical model, a main sequence 06-07 star ($T_\star=41000$ K, $L_\star=2.5\times 10^5 L_\odot$) in a dust cocoon extending from 0.0001 pc to 2.5 pc, with a smooth-to-clumpy ratio of 0.1 and fractal dimension 2.6. The cocoon is representative of the inferred properties of massive YSOs: a thousand solar masses of dust in about a 1/3 parsec region. (At typical Galactic distances of 5kpc, 1/3pc=13'' and 2.5pc=100'') As massive YSOs can heat a large part of their natal clouds, we chose to include the larger envelope out to 2.5pc and 50000 M_\odot ; this does not qualitatively affect our conclusions. The visual extinction averaged over all sightlines is $A_V=131$, but varies between 13 to 401 magnitudes depending on viewing angle. The voids at small radii allow stellar radiation to propagate further, heating the inner faces of clumps. This can result in a greater mass of warm dust than if all of the stellar optical and UV radiation was intercepted near the star; in other words, the $\tau_V = 1$ surface is irregular and will enclose a different amount of mass than in a spherically symmetric model. This is clearly visible in

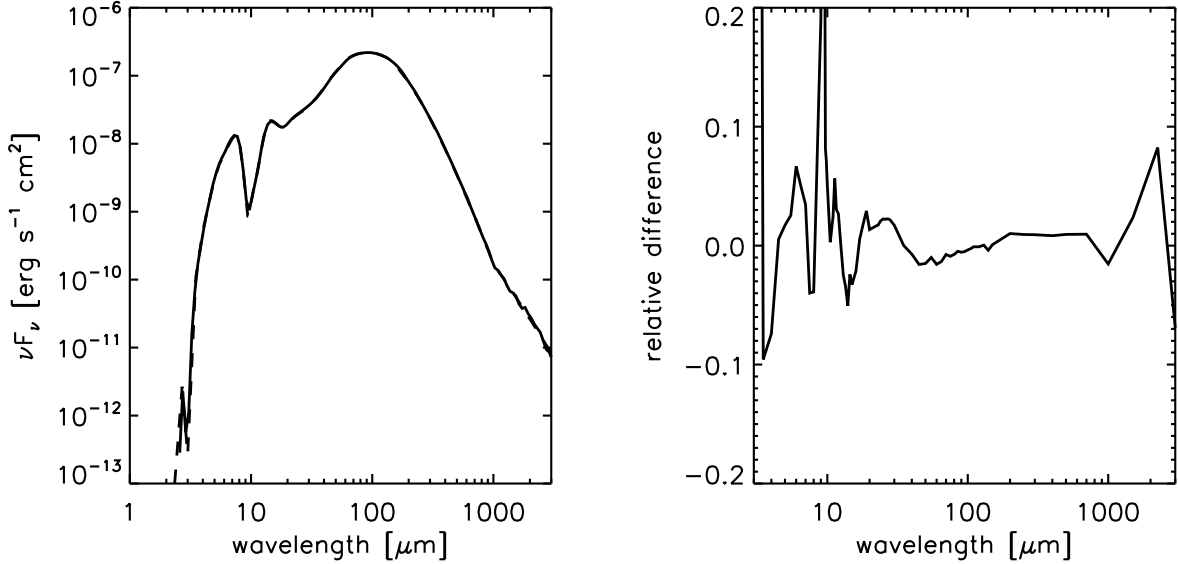


Fig. 1.— The first panel shows a 1-D model (spherically symmetric) calculated with our code (solid line) and DUSTY (dashed line). The source is a main sequence 06-07 star ($T_\star=41000$ K) in a $50000 M_\odot$ dust cocoon extending from 0.0001 to 2.5 pc. The optical depth of the cocoon is $\tau_V=117.5$, and the temperature on the inner radius is 700 K. The second panel shows the fractional difference between our model and one calculated with DUSTY. Variations of a few percent are mostly due to noise in our spectrum.

the temperature map, which shows cool dust in the shadows of clumps, and heated inner surfaces.

The radial temperature profile is sometimes used as a diagnostic when young stellar objects are modeled. As one would expect, the radial temperature profiles for clumpy models vary greatly depending on the placement of the clumps of dust. Even the radial temperature profiles averaged over all angles show significant variation with the particular clump geometry, and differ from the profile of a smooth (1-D) model with the same amount of circumstellar mass. Figure 3 illustrates this comparison with smooth and clumpy models that have the same amount of circumstellar mass. The smooth model's temperature gradient is shallower than the clumpy models in the inner regions, because the clumpy models tend to have lower average density there. However, a smooth model with a completely evacuated hole out to the distance of the nearest dense clump in the clumpy models also shows a faster temperature dropoff than the clumpy models. This is the effect mentioned above, that the $\tau=1$ surface for intercepting stellar radiation is irregular, and clump surfaces can be heated at larger distances from the star than in a spherically symmetric model with the

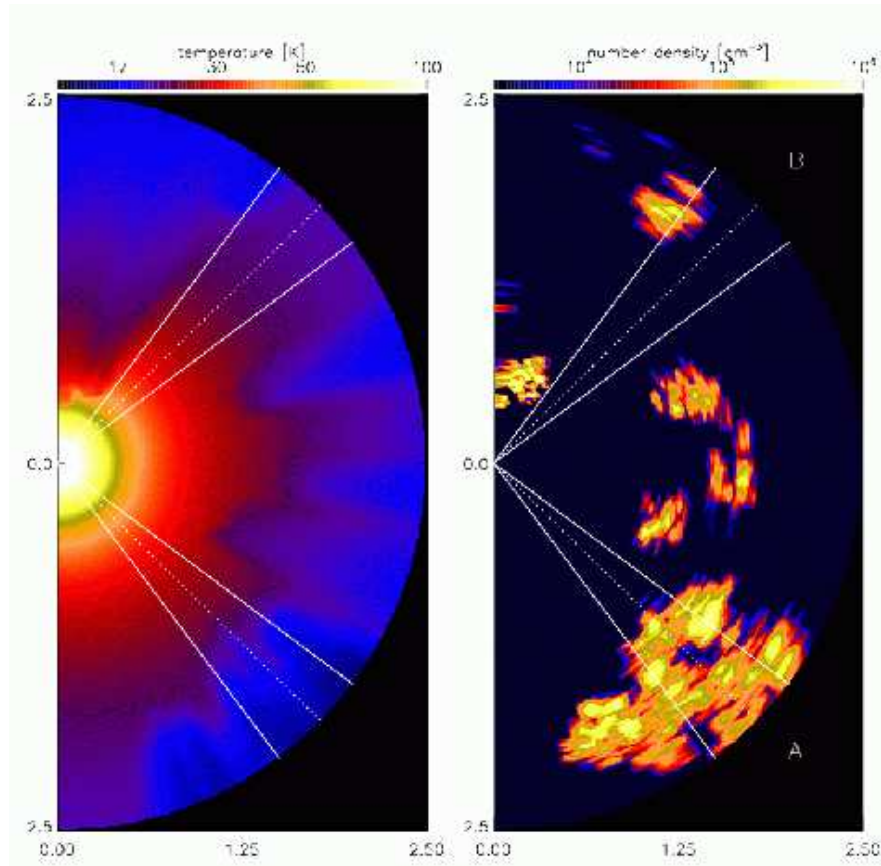


Fig. 2.— Density and temperature distributions in a slice of a typical model. Both quantities are shown on a logarithmic scale, with the ranges shown by the color bars. The spatial scale is in parsecs. Two particular sightlines discussed in the text (“A” and “B”, §3.4) are shown as dotted lines (although we will discuss a sightline as if it were a single viewing angle, radiation leaving the simulation is binned over the finite range of angles indicated by the solid lines).

most similar radial dust distribution. For the dust used here, temperature is expected to drop off as $r^{-0.33}$ or $r^{-0.4}$ in the optically thin and thick smooth cases, respectively (more discussion in Whitney et al. 2003a). The different slopes for different clumpy models likely reflect transitions between optically thin interclump material and optically thick clumps.

3.2. SEDs

We show here a comparison of SEDs of the clumpy and smooth model for our canonical parameter set discussed in § 2. As Figure 4 shows, our clumpy model differs from the smooth model most significantly in the NIR and MIR. The voids between the clumps (Figure 2) allow NIR flux to scatter through and escape the envelope. MIR flux also can escape along certain sightlines. The $10\ \mu\text{m}$ silicate feature varies greatly between the different sightlines of the clumpy model, but the average depth is lower than that of the smooth model. The slope of the SED in the NIR and MIR is flatter on average in the clumpy model than the smooth. As we will show in later sections, these two features of the clumpy models agree better with observational data of several UCH II sources.

Figure 2 showed a slice of the density and temperature structure for a typical clumpy model, with two particular sightlines marked. The SEDs for all 200 sightlines in this model are shown in Figure 4 (in gray), with the two sightlines highlighted. The output spectra are binned over a finite range in angle, indicated in Fig. 2 for each sightline by two solid lines bracketing the dotted line. It is important to remember that although we have only shown the sightline intersecting the central source, the SED at each viewing angle is due to emission in that direction from the entire object, i.e. all rays parallel to the range of angles indicated. The SED with lesser near-infrared flux corresponds to the lower (“A”) of the two sightlines in Fig. 2 – there are clumps in the outer envelope in this direction that obscure the inner regions (this cooler dust also causes the $10\mu\text{m}$ silicate absorption present in the SED, Fig. 4). Along the upper sightline “B”, there are few clouds at a radius greater than 0.4 pc, and much more NIR radiation can scatter out from the inner regions (dashed SED, Fig. 4). The orientation of the two sightlines is particular to this model – there is no preferred direction to the clump distribution in general.

3.3. Synthetic Images

Figure 5 shows 3-color images of our canonical clumpy model as it would be imaged with a standard ground-based NIR camera, and with the IRAC and MIPS on *Spitzer*. Specif-

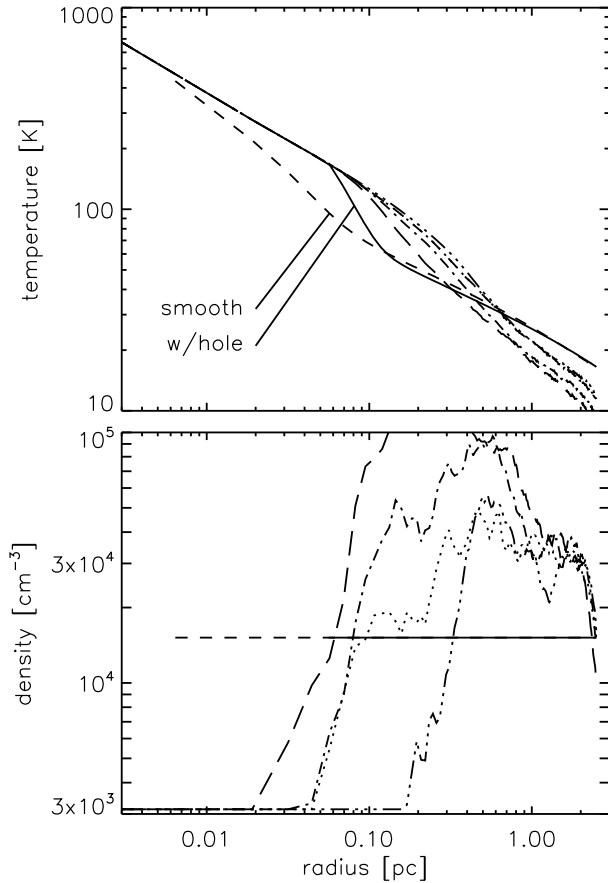


Fig. 3.— Comparison of spherically-averaged radial temperature and density profiles for smooth and clumpy models. All models shown here have the same amount of circumstellar dust within the same 2.5 pc radius. Two smooth models (solid and dashed lines) and 4 clumpy models (long dashed, dot-dashed, dotted, and triple-dot-dashed lines) are shown; the density and temperature profiles for the clumpy models are averages over all angles. The upper plot shows the temperature profiles, and the lower the corresponding density profiles. The smooth model which extends all the way to the dust destruction radius at constant density (dashed line) has the shallowest gradient, because it has the highest density in the inner regions of the four clumpy models. The temperature of a smooth model with a completely evacuated inner hole (solid line) also falls off faster with radius than any clumpy model, because the inner faces of clumps at varying distances are illuminated and heated, whereas all stellar radiation of a given wavelength is intercepted at the same radius in a smooth model.

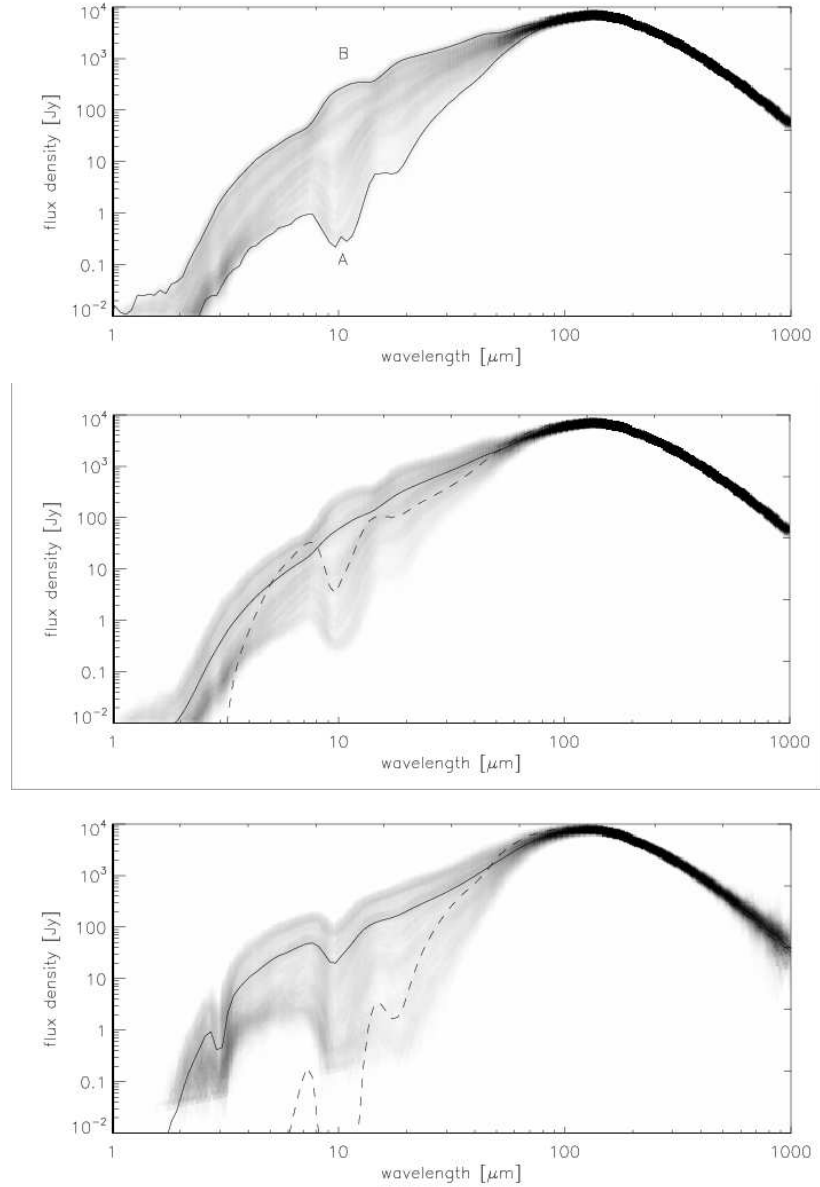


Fig. 4.— SEDs of clumpy and smooth models. The first panel shows the range of SEDs for different sightlines of the canonical clumpy model. The grey scale is darker where more similar SEDs coincide. SEDs of two particular sightlines (“A” and “B”, see Figs. 2 and 5) are highlighted. The second panel compares the clumpy model to a smooth model (dashed line) with the same dust mass and inner and outer radii. The average sightline of the clumpy model is shown as a solid line. The third panel makes the same comparison between a clumpy and smooth model, but now with an average radial density power-law gradient ($\rho \propto r^{-1}$). For simplicity we mostly discuss the differences between smooth and clumpy models with no radial dependence of the average density. In the model with a gradient, the differences are even larger - both models have higher average optical depth (than the models without a radial gradient) and more hot dust close to the star emitting in the NIR, but that emission only escapes and is observable in the clumpy model, which has low-density sightlines. In the smooth model all of that extra emission is preprocessed further out in the envelope.

ically, the images are constructed by convolving the simulated output radiation field with the (J,H,K_s), ([3.6],[4.5],[8.0]), and ([24],[70],[160]) filters. The top row shows a spherically symmetric model, and the second two rows are a clumpy model viewed from different angles. Clearly, the greatest difference is in the near-IR – the clumpy model is >6 orders of magnitude brighter at these wavelengths. The clumpy model is also brighter in the mid-infrared (IRAC wavelengths), but more striking is the very different color – the smooth model is much redder, with higher average extinction than the clumpy model, and cooler dust farther out in the cocoon on average. Differences are less significant at longer wavelengths, which mostly trace the total dust mass, and are less sensitive to its distribution. This agrees with the SEDs shown in Figure 4.

3.4. Integrated SED

Not only does the shape of the spectral energy distribution change with viewing angle, but the total wavelength-integrated flux can change significantly as well. Figure 6 shows contours of the bolometric flux as a function of ϕ and θ , the azimuthal and polar/altitude viewing angles, for a typical clumpy model. The luminosity that an observer would calculate by (incorrectly) assuming isotropic emission varies from 60% of the true luminosity along some sightlines to nearly twice the true value along other sightlines. The “dim” sightlines are those along which a dense clump is located at a moderate to large distance from the central source. Dense clumps along one’s sightline, but very close to the central source, do not necessarily result in an overall dimming, because short-wavelength light can scatter around the clump, the viewer may still be able to see uneclipsed hot dust in the cocoon. We note that this variation of the bolometric flux was also found in the low-mass protostar model of Whitney et al. (2003a).

3.5. Colors

Observationally, the SED of young stellar objects is usually only sampled with a few broad-band filters, so it is important to show how the variation apparent in Figure 4 translates into a range of photometric colors. With the successful launch of *Spitzer*, the availability of 2MASS, and widespread access to deep near-infrared imaging, photometry of a great number of young stellar objects is available in the 10 filters J , H , K , IRAC [3.6], [4.5], [5.8], and MIPS [24], [70], [160], so we concentrate on these (though we note that in many cases the 160 μ m band is not very observationally useful because of its low resolution and saturation limit). For conversion of fluxes to magnitudes we use 1594., 1083., and 666.7 Jy for 2MASS

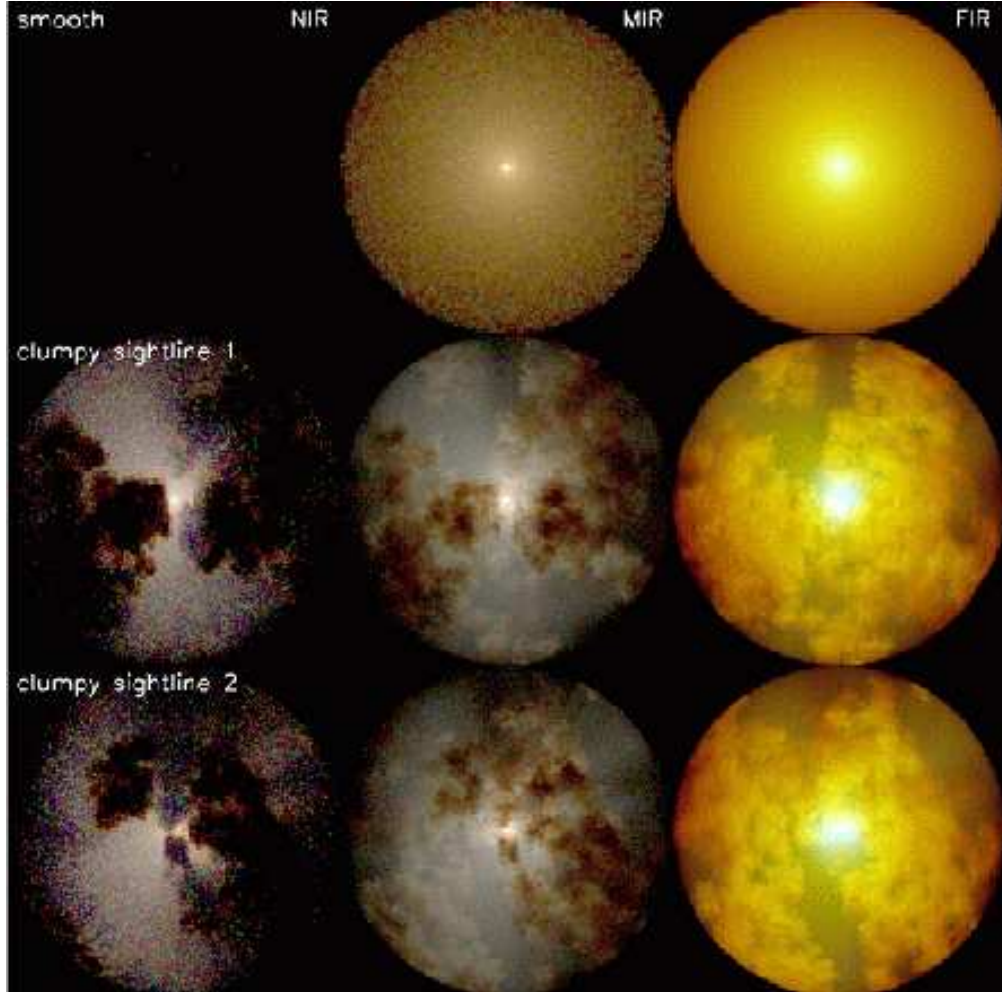


Fig. 5.— Synthetic 3-color images of a massive star embedded in clumpy cloud. The top row is a spherically symmetric model, and the second two rows are two views of a clumpy model with the same mass of circumstellar dust. (The two sightlines are those marked in Figure 2.) The NIR (left panels) images are composed of the emergent spectrum convolved with the 2MASS J,H, and K_s filters as blue, red, and green respectively and a logarithmic stretch. The MIR (center panels) images are similarly composed from synthetic IRAC [3.6], [4.5], and [8.0] images, and the FIR (right panels) images from synthetic MIPS [24], [70], and [160] images. We have not convolved these images with *Spitzer* resolution (1.5'' at 6 μ m and diffraction limited at higher wavelengths); the effect would be negligible for the NIR and MIR image, but would begin to strongly affect the FIR image at the assumed distance of 5 kpc.

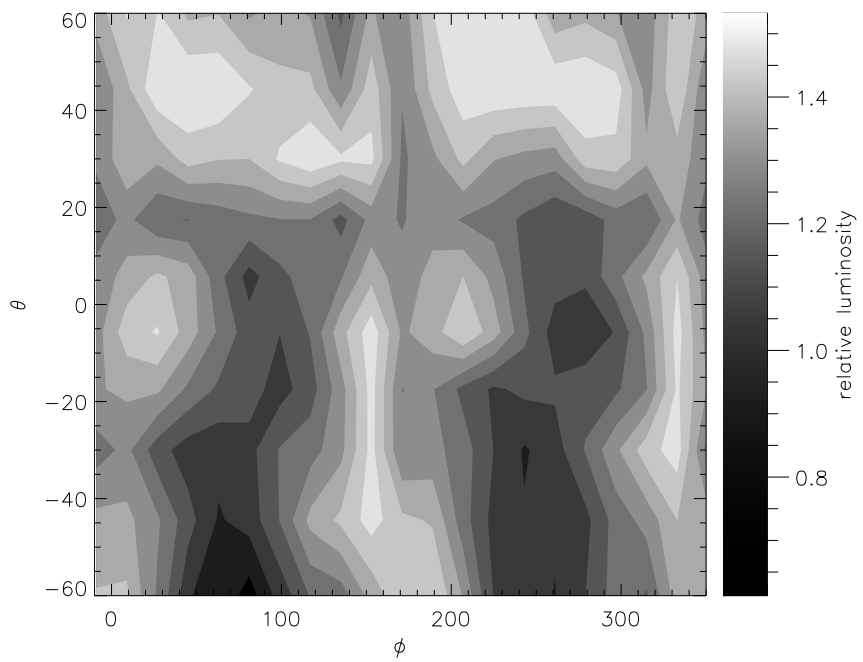


Fig. 6.— Observed bolometric flux as a function of polar/altitude (θ) and azimuthal (ϕ) viewing angle. The light spots are angles along which the observed luminosity (if the observer assumes isotropic emission) is twice the true value, and in the dark regions the observed value is 60% of the true value.

J , H , and K_s , 277.5, 179.5, 116.6, 63.1, and 7.16 Jy for the four IRAC bands and MIPS [24] (M. Cohen 2004, private communication), and an estimated 0.75 and 0.2 Jy for MIPS [70] and [160]. We also calculate the IRAS fluxes of our models and discuss these briefly in §5.

Figure 7 shows two color-color diagrams for our example typical clumpy model, viewed from 200 different angles. The near-infrared bands vary the most with viewing angle, but colors formed with an IRAC band and MIPS [24] are also quite sensitive to the circumstellar dust distribution. This is because the MIPS bands are at long enough wavelengths that they sample predominantly thermal emission of fairly cool dust; the flux density mostly depends on the total dust mass and is less affected by the particular distribution. We also show the color-color diagram formed exclusively from IRAC bands, since many young stellar objects in the inner Galaxy are being imaged with IRAC by the GLIMPSE survey (Benjamin et al. 2003; Churchwell et. al 2004; Whitney et al. 2004a). Colors can vary with viewing angle by more than a magnitude for the same object. The corresponding smooth model (same dust mass and inner and outer radii) is shown on the two CCDs, indicating that even though the variation between sightlines in the clumpy model is large, the difference between any sightline and a smooth model is even larger. The smooth model is extremely embedded and nearly invisible in the NIR, so the [K]-[3.6] color is far off the right side of the first panel. Even the IRAC-only colors of the smooth model are different from the clumpy model by more than a magnitude.

3.6. Fitting 3-D data with 1-D Models

The spectral energy distributions of 3-D clumpy models are significantly different from those of 1-D smooth models. We attempt to fit the output of our 3-D models with 1-D models, revealing several specific differences: 1) The derived physical parameters (dust mass, etc) are often very different, 2) the derived physical parameters for the same object depend on viewing angle, and 3) sometimes it is impossible to fit the (synthetic) data with a 1-D model at all. Figure 8 illustrates these points. The range of SEDs for a single clumpy model seen from different angles is shown as a gray scale, along with three 1-D models. The “true” physical parameters are $50000 M_\odot$ of circumstellar material around an O-type star ($T_\star = 41040$ K, $L_\star = 2.54 \times 10^5 L_\odot$). Some very thin dust extends all the way in to 0.0001 pc (the density is never truly zero), and the closest clump (typical density of clumps is 10^5 cm^{-3}) is at radius 0.035 pc, and temperature 250 K. The average optical depth to the central star is $A_V = 131$, but that quantity ranges from 13 to 401 magnitudes depending on viewing angle.

We have concentrated here on fitting the NIR and MIR parts of the SED, without heavily constraining the FIR. This is motivated by current observational capability, which

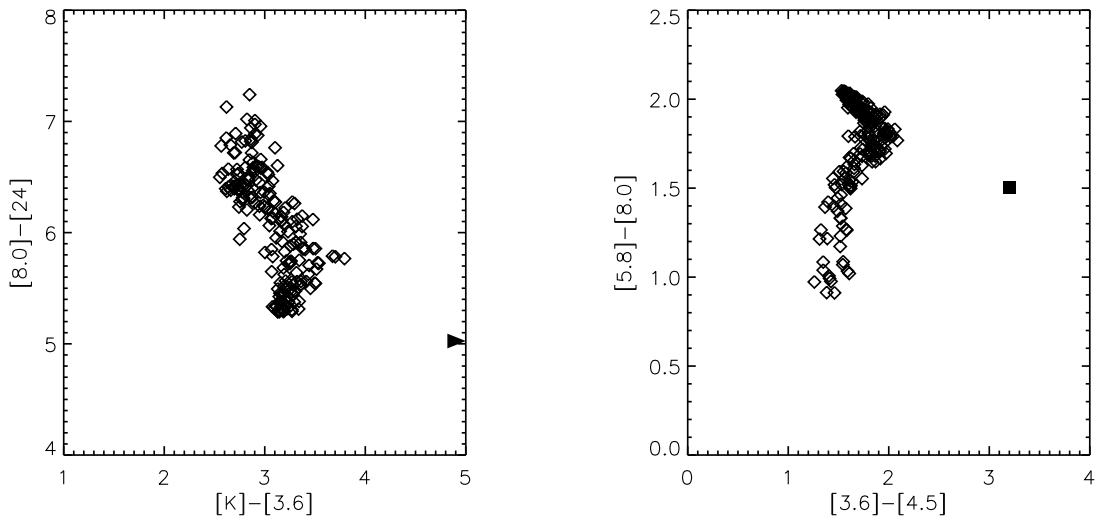


Fig. 7.— Color-color diagrams (CCDs) for different observations of a *single* modeled object, an 0-type star with $50000 M_{\odot}$ of circumstellar material distributed in clumps between 0.0001 and 2.5 pc radius (the same model as Figs. 2-6). The different points are for the 200 different viewing angles calculated for each model. In the first panel, colors across the broad wavelength range $2-25\mu\text{m}$ are shown, and in the second panel colors derivable exclusively from IRAC photometry. The corresponding smooth model is shown as a filled triangle in the first panel, indicating that the actual point is far off the plot to the right, and as a filled square in the second panel.

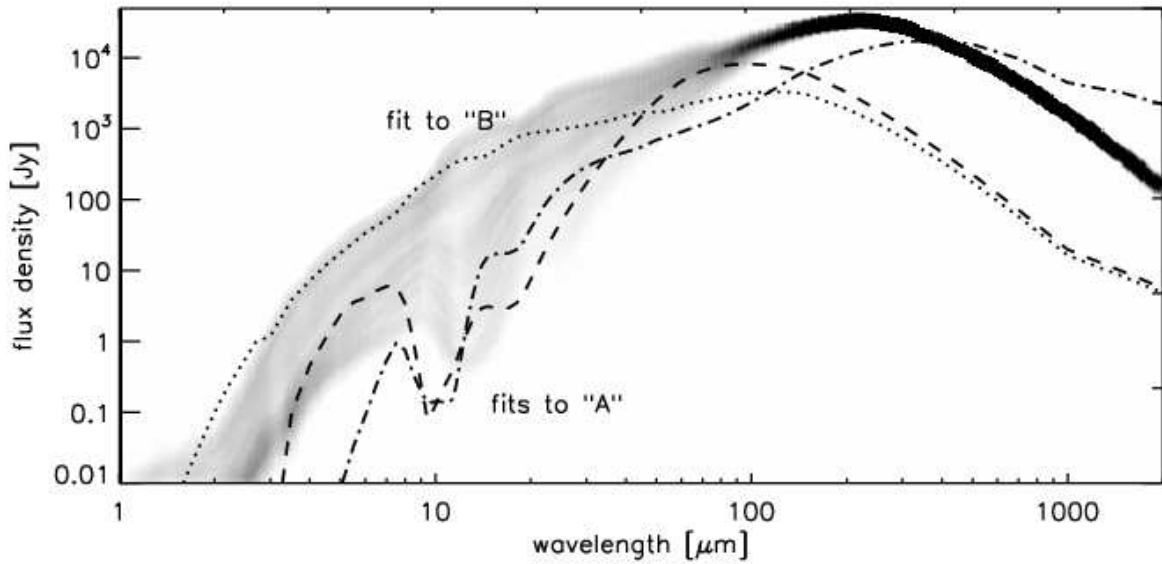


Fig. 8.— Attempted 1-D fits to the SEDs of a 3-D clumpy model. The variation of SEDs with viewing angle is shown in grayscale as in Figure 4. The high and low extremes of the grayscale correspond to the two sightlines shown in Fig. 2 that have particularly high and low NIR flux densities (“B” and “A”, respectively, see first panel of Fig 4). The dotted line is the best 1-D fit to SED “B”. The dashed and dot-dashed are 1-D fits to SED “A”. The 1-D model parameters do not reflect the true dust distribution very closely – see text for more discussion.

includes the widespread availability of NIR spectrographs and cameras and *Spitzer*’s relatively high-resolution coverage of 3-30 μ m. IRAS and even the 70 and 160 μ m channels of MIPS on *Spitzer* are resolution-challenged, and it is more difficult to draw conclusions about massive protostars (generally at distances >1 kpc and in crowded environments) from these instruments. One can instead try to crudely fit the shape of the entire SED using a 1-D model; a reasonable match to the SED shape can be made for the least embedded sightlines as shown below. However, in general these 1-D fits either fail to reproduce the 10 μ m silicate feature in absorption or have MIR ($\sim 5\mu$ m) fluxes that are 1-3 orders of magnitude too low, and more seriously, the physical parameters derived are not the same as the 3-D model (size and mass of the cocoon).

In order to quantify the differences between the SEDs produced by smooth 1-D and clumpy 3-D models, we constructed a grid of 5000 smooth models, varying the inner and outer radius, the optical depth or dust mass, and the radial density profile (power-law profiles $\rho(r) \propto r^\alpha$). We then calculated the “ χ^2 ” goodness-of-fit between each 1-D model and a selected 3-D sightline (and below, observation of a real YSO). We used an arbitrary “uncertainty” of 0.1 dex to calculate χ^2 for the model SEDs – the preferred parts of parameter space are not affected by this choice. Figure 9 shows this goodness of fit as a function of the optical depth τ_V , the inner and outer radii r_{in} and r_{out} , and the radial density power-law index α .

The dotted line shows the best 1-D fit to the 3-D sightline with particularly high NIR/MIR flux density (“B” in Fig. 2). The best fitting models have fairly flat radial density profiles ($\alpha = 0.0$; fit parameters are listed in Table 1). The preferred optical depths are much lower than the average optical depth of the 3-D model (21% for this best-fit model), so the dust mass would be severely underestimated. If one decreases the optical depth in the smooth model in order to increase the flux density at shorter wavelengths, one is also forced to increase the outer radius and total dust mass to maintain the observed FIR flux density. It is difficult to produce sensible 1-D models that have the 10 μ m silicate feature in emission as well as the shape of the SED at other wavelengths (in the 3-D models this is possible for viewing angles at which very hot dust near the star is not severely obscured.)

It is even more difficult to fit the sightlines like “A” that have low MIR intensity using a 1-D model. The dot-dashed line shows the best fit constant-density model, which has a reasonably deep silicate absorption feature but not enough NIR flux and too much flux at 20 μ m. This is a general feature with 1-D models that try to mimic typical sightlines of the 3-D model: the optical depth must be kept moderate (similar or somewhat greater than the average value of the clumpy models) to produce the silicate absorption feature, and then there is no way to get emission shortward of 2 μ m out of a reasonably embedded source

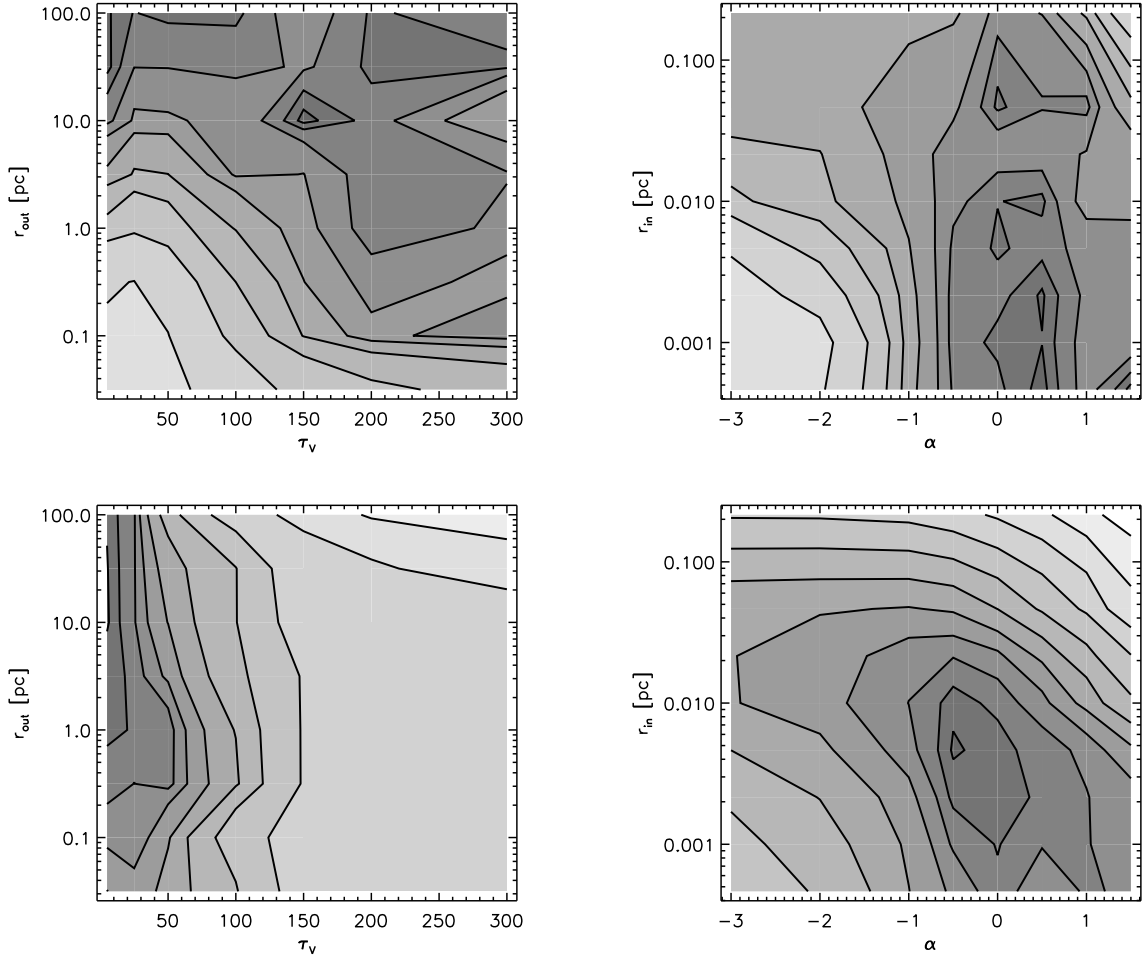


Fig. 9.— Goodness of fit of 1-D smooth models to two selected 3-D clumpy SEDs. The first two panels represent attempts to fit sightline “A” with a strong silicate absorption feature. The second two panels are for sightline “B” which shows silicate emission. In both cases, sightlines with fairly flat radial density profiles and larger inner and outer radii than the true model are preferred. The best fits have fairly poor “ χ^2 ” values of 5 – 10.

Table 1. Parameters of 1-D models fitting 3-D models

model	density index α^a	r_i [pc]	r_o [pc]	mass M_\odot	luminosity $10^5 L_\odot$	Average Av to star	“ χ^2 ”
clumpy	0	0.0001 ^b	2.5	50000	2.54	131	–
1-D fits to lower sightline “A”							
dashed line Fig 8	0	0.047	47.	2.9×10^7	2.54	217	8.7
dot-dash line Fig 8	+1.5	0.00039	12.	2.0×10^6	2.54	163	4.8
luminosity unconstrained	0	0.0005	91	5.6×10^7	0.6	109	–
	-1	0.0070	7.0	1.4×10^5	0.5	200	–
1-D fits to upper sightline “B”							
dotted line Fig 8	0	0.0027	2.7	2.3×10^5	2.54	27	8.2
luminosity unconstrained	0	0.0023	3.5	31300	3.5	43	–

^aSmooth models were run with a power-law density gradient $\rho \propto r^\alpha$.

^bClumpy models have diffuse material extending in to the dust destruction radius, but the distance to the nearest dense ($\gtrsim 10^5 \text{ cm}^{-3}$) clump is farther out (0.035pc).

without an inhomogeneous envelope. In 1-D models the depth of the silicate feature is tied to the mass of the envelope, but three dimensions these are decoupled.

The best-fitting models also have unreasonably large outer radii, and often, large inner holes or radial density profiles that increase with radius (a low-density inner region is similar to a hole of zero density). It is these last models (positive α) which produce the peak in the goodness-of-fit at very low τ and very large r_{out} – we do not consider these models physically reasonable, but plot one for completeness (dashed line). We note that 1-D fits to real data have the same characteristics – flat radial profiles and large outer and inner radii. (Our fits are discussed below, others such as F98 found the same result.)

If one did not know the intrinsic luminosity of the source, that parameter would also likely be fit incorrectly. We did not construct a full grid of models with different luminosities, but explored a range of parameter space fitting by eye, and found that the fit could be improved slightly over the SEDs shown in Figure 8 by changing the source luminosity (downward for sightline “A” and upward for sightline “B” – those model parameters are also listed in Table 1). We will see in later sections that 1-D models face similar difficulties in fitting real data that they do in fitting 3-D SEDs.

4. More General Clumpy Models – Observable Trends

4.1. Relating the SED and the dust distribution

Although the same young stellar object can look different depending on the viewing angle, trends do exist that are strong enough to overcome that intrinsic scatter and probe the physical state of the circumstellar dust. Spatially averaged information about the density distribution and size of the inner cavity, the magnitude of density fluctuations relative to the mean, and the total dust mass are all observationally accessible.

4.1.1. Trends with average A_V and inner cavity size

One intuitive fact about circumstellar dust that remains true even in the presence of complex density distributions is that as the optical depth to the source of emission increases, the emergent near- and mid- infrared light decreases and the source appears redder. If one considers different sources with the same mass of circumstellar dust, then the size of an inner cavity or hole should be anticorrelated with the optical depth to the central source. In clumpy models, there is not a spherical inner hole, but the average distance of dust

from the central star varies depending on the specifics of the clump distribution. We can explore this effect in a natural way by running many models with different random seeds or realizations of the clump distribution. Figure 10 illustrates the results: We show 100 models with a smooth-to-clumpy ratio of 0.1 (mostly clumpy), and different random seeds of the clump distribution. The 20000 SEDs (200 viewing angles per model) vary widely at the shorter wavelengths, and the [5.8]-[24] color shown in the lower panels can vary by over two magnitudes for a single model. The expected trend is nevertheless visible - models in which the clumps are largely further from the central source have somewhat lower average optical depth, and are somewhat bluer. The trend is quite clear in the angle-averaged properties of models (see the five highlighted models in particular), but the angle-averaged properties are not observable from Earth.

The effective fractal dimension D offers another way to quantify the dust distribution – a larger effective dimension corresponds to more “fluffy” clouds with a larger filling factor. Most of our models use $D=2.6$, close to the effective dimension suggested by Elmegreen & Falgarone (1996) for the general interstellar medium, but we verify here that within a reasonable range, this choice does not have a strong effect on our results. Figure 11 shows slices of models with higher and lower D , as compared to the standard shown in Fig. 2. The SEDs and properties of models with a range of D are shown in Figure 12, where as before the full range of sightlines is shown and selected angle-averaged properties are highlighted. The variation of observable properties (SED, colors) is less than the variation as one changes the viewing angle for a single model. A fluffier or more filled cloud distribution results in somewhat redder colors and larger average optical depth, which is not surprising, but the effect is smaller than others examined in this paper, such as the cloud/intercloud density contrast (smooth-to-clumpy ratio).

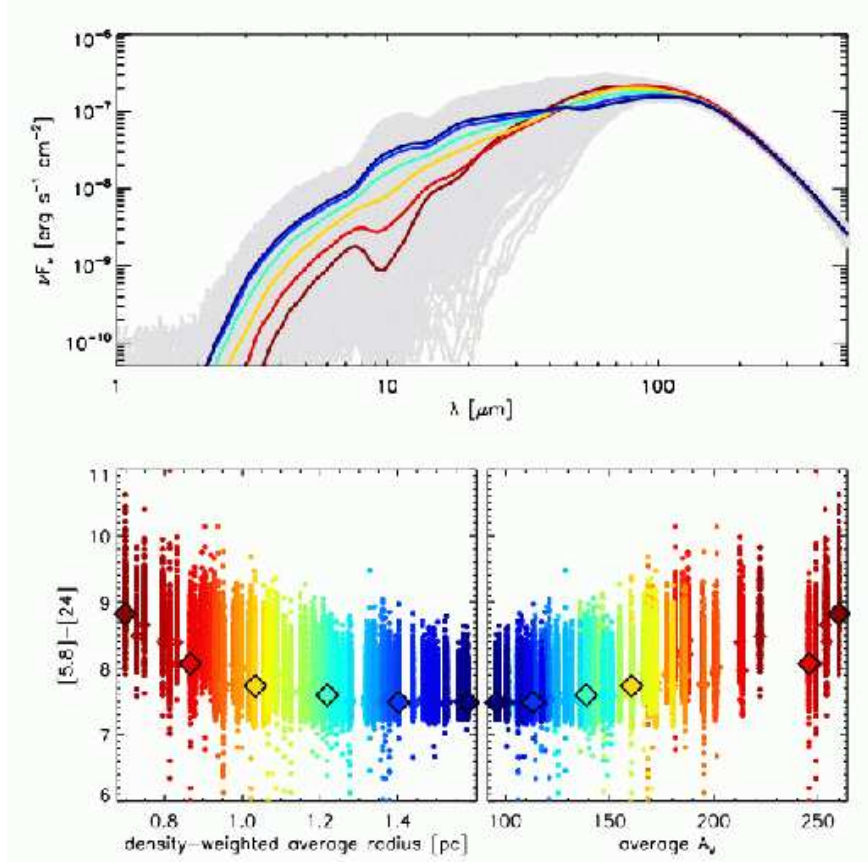


Fig. 10.— One hundred clumpy models with the same amount of circumstellar mass in different random clump distributions. The upper panel shows the range of the 20000 sightlines (200 per model) as gray lines. Five particular models have been highlighted in color, and the *angle-averaged* SED plotted for those five. The lower panels show how the $5.8\mu\text{m}$ - $24\mu\text{m}$ color varies as a function of the density weighted average radius (a measure of the distance from the central source at which most of the dust is located) and of the angle-averaged optical depth to the central source. The 200 sightlines for each model are marked as dots in the lower panels, and the angle-averaged properties of the five highlighted models are shown as large diamonds.

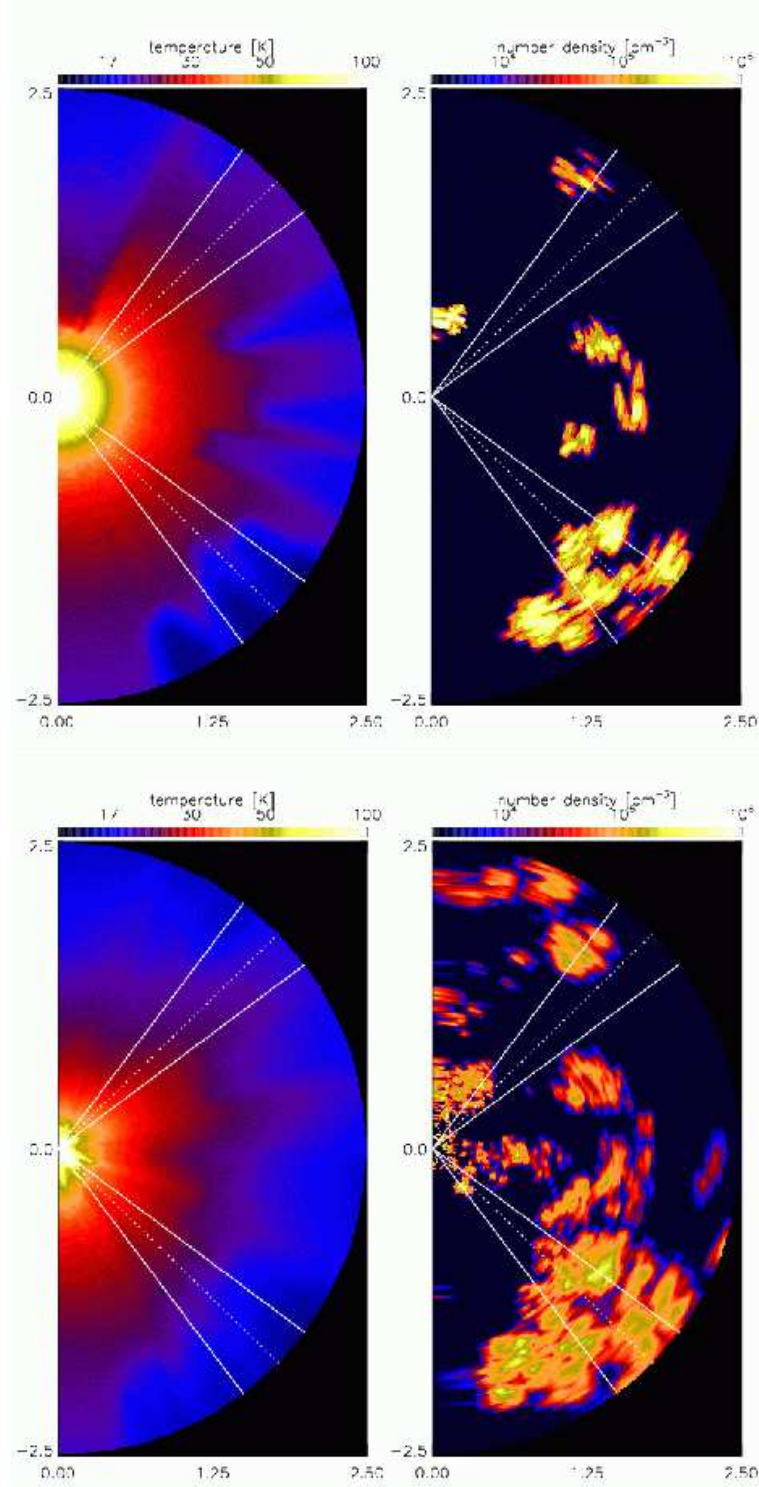


Fig. 11.— Models with effective fractal dimensions $D=2.4$ and 2.9 - compare to Fig. 2, which has $D=2.6$, the standard used in most of our models. Higher effective fractal dimension corresponds to “fluffier” clouds, a more filled cloud distribution, and lower density peaks.

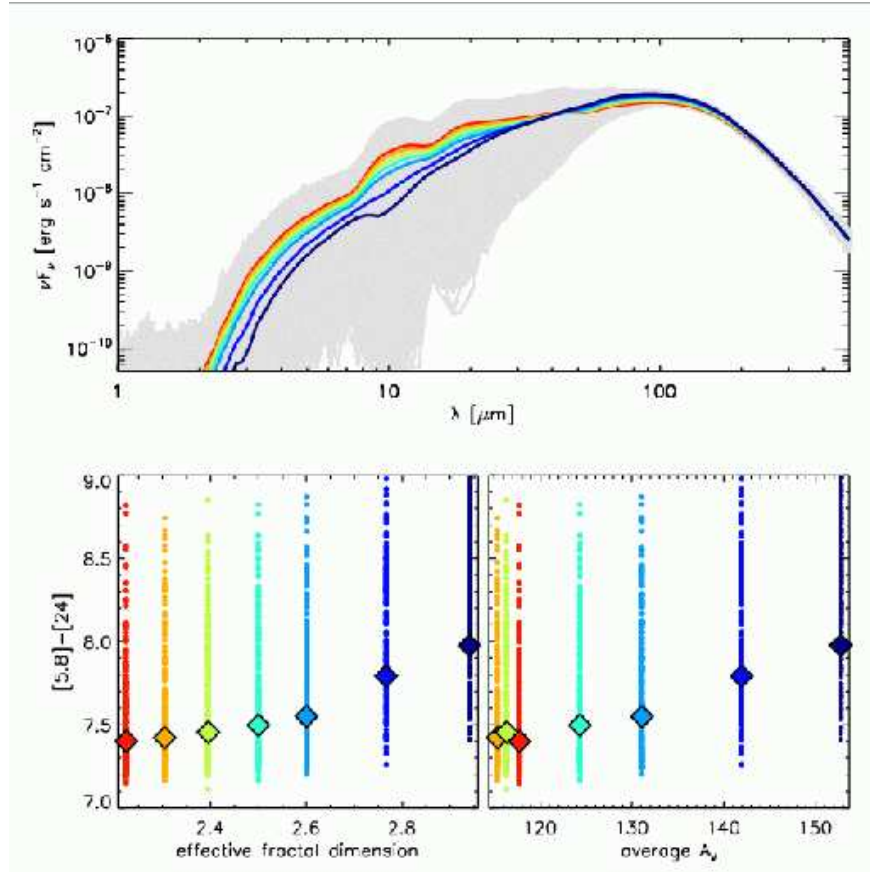


Fig. 12.— The effective fractal dimension D does not have a strong effect on results (within the range shown, which is believed to be the relevant range for the ISM). The 200 sightlines for each of 7 models with different D are shown as gray scale in the upper panel, and dots in the lower panel. The angle-averaged properties are shown as thick SEDs and large diamonds. The variation in observable properties with D is less than the variation of a single model with viewing angle.

4.2. Trends with smooth-to-clumpy ratio

To quantify the effects of a clumpy circumstellar medium in another way, we varied the ratio of the typical clump density to that of the smooth interclump medium. Figure 13 shows the effect of varying the smooth-to-clumpy ratio for models the same particular random distribution of clouds. As in similar figures above, we show the range spanned by different viewing angles as well as the average properties to highlight the trend. As the smooth-to-clumpy ratio increases, the depth of the $10\mu\text{m}$ silicate feature increases, and the models become redder shortward of that feature. The MIR flux actually increases slightly for some parts of parameter space: the clumpy models can have a central hole with fairly thin material if there is not a clump immediately near the star, or a similar effect occurs if there is a clump at small radii but only one side of the star. The effect of making such a model smoother is in fact to fill in that inner region with denser material, which can increase the mass of warm dust. In the smoother models, however, much of the radiation from such dust (at wavelengths shortward of a few microns) is extinguished and reprocessed back in the far-IR part of the SED (see the rise in the peak at $\sim 100\mu\text{m}$ in Figure 13). The result is commonly the relative lowering of the $20\mu\text{m}$ and NIR fluxes as shown in the Figure. Although there are large variations with viewing angle, the smoothness of the cocoon has a large enough effect that it can be observationally probed. To further illustrate that, we ran many models with different smooth-to-clumpy ratios and different random clump distributions. Figure 14 shows the results. Particularly if one can observe a *sample* of similar objects, the mean color of the sample will reflect the smoothness of the circumstellar dust distribution – we will demonstrate in the next section.

5. Comparison with data

Now we apply the lessons of the previous section to real datasets, to determine what we can learn about the physical properties of ultracompact H II regions (embedded massive protostars) using our clumpy models. Wood & Churchwell (1989) (hereafter WC89) examined the IRAS colors of ultracompact H II regions and determined that objects in a sufficiently red part of color space were likely to be massive protostars. This criterion has been used widely as the starting point for surveys of protostars and protostellar candidates, including thermal and maser molecular line targeted observations and imaging from radio continuum through the infrared. Although higher resolution more sensitive infrared data (MSX and *Spitzer*/GLIMPSE) is beginning to become available, IRAS is still a cornerstone dataset for studying dusty Galactic objects, so we calculate and describe the IRAS fluxes and colors of our models here. Figure 15 shows a color-color diagram similar to that of WC89. The WC89

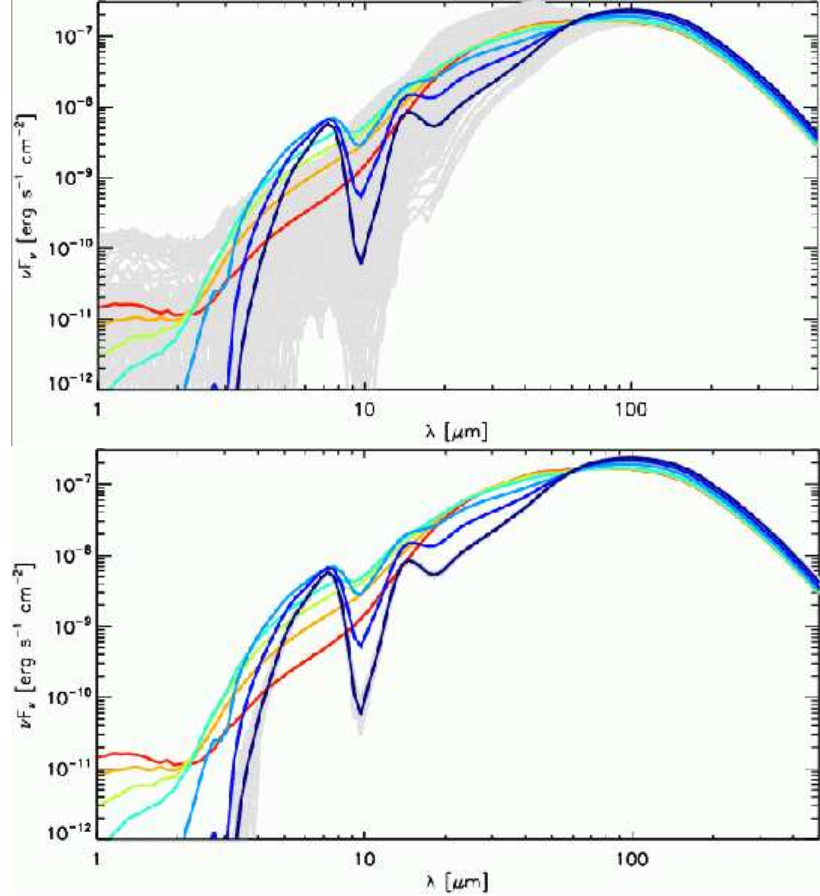


Fig. 13.— SEDs for models with different ratios of smooth to clumpy density distribution, from completely clumpy (lightest gray; red in color version) with nearly evacuated voids to completely smooth (darkest gray; dark blue in color version). Each colored line in the upper plot represents the average of 200 viewing angles, and the gray scale shows the range spanned by those individual sightlines (as the average sightline is not observable from earth). In the upper plot the gray scale is the range spanned by the model with 1% smooth-to-clumpy ratio (very evacuated voids), and in the lower plot the gray scale is for the 90% smooth model. Although there are still large variations with viewing angle, the smoothness of the cocoon is a large enough effect to be observationally probed.

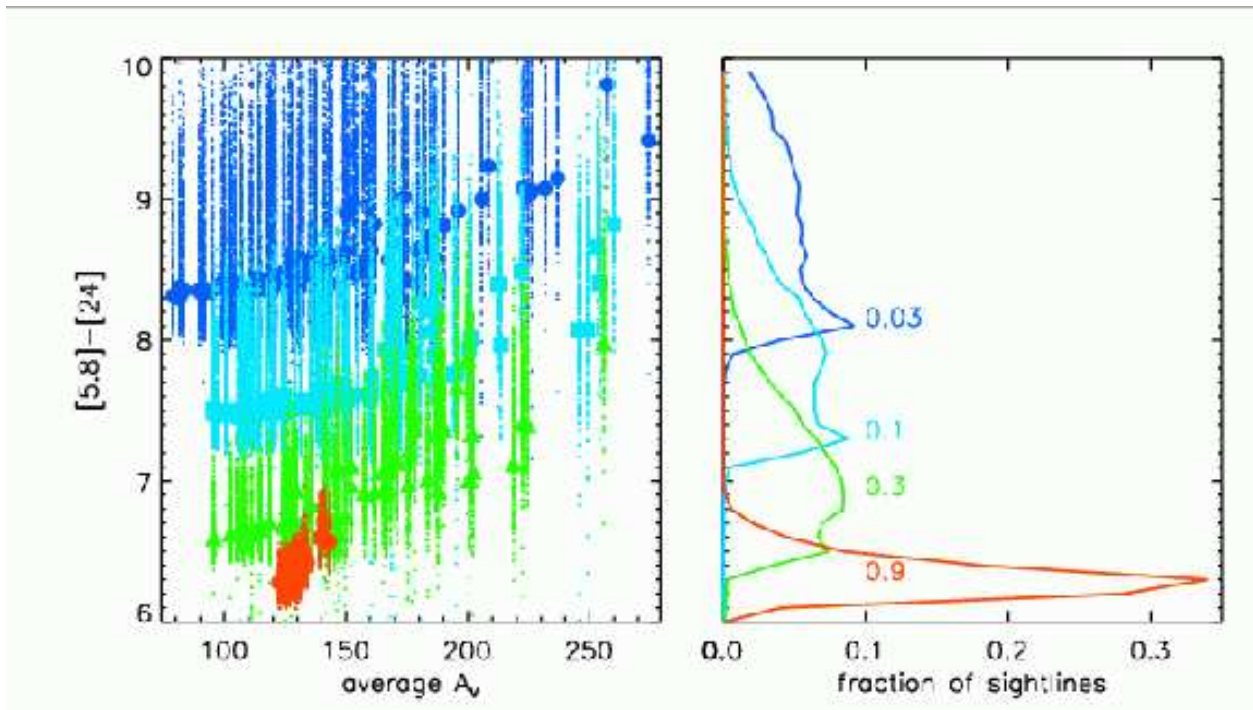


Fig. 14.— The left panel of this figure is similar to the lower right panel of Fig. 10, showing 244 models with different distributions of the same total mass of clumpy clouds, but here different ratios of smooth to clumpy material are shown, 0.03 (blue circles), 0.1 (squares), 0.3 (triangles), and 0.9 (red circles). The right panel collapses the horizontal axis, showing histograms of the observable quantity, [5.8]-[24] color, labeled according to smooth-to-clumpy ratio. Clearly, the color can diagnose the degree of clumpiness of the medium (if the luminosity of the central source is known and the total mass can be estimated e.g. from FIR observations).

color box is plotted along with the colors of field objects and UCH II regions. The latter are from the survey of Kurtz et al. (1994) that includes the WC89 sample as a subset. Our models have IRAS colors that fit the WC89 criteria, but smooth models do also. The colors are shown along different sightlines for a model with smooth-to-clumpy ratio of 0.03, 0.1, and 0.9. In this part of parameter space (hot protostars with a circumstellar dust cocoon about a parsec in size with mean density a few times 10^4 cm^{-3}), making the cocoon smoother or increasing its density while maintaining the same size both result in bluer [12]-[25] colors, but not much change in [60]-[12]. Decreasing the total mass without changing the average density (a smaller envelope) results in bluer [60]-[12] without a large change in [25]-[12].

Spectroscopy can almost always constrain models more tightly than photometry, so we next compare against ground-based MIR spectroscopy of UCH II regions by F98. We begin with G5.89-0.39, an UCH II which was given special attention by those authors and which had been modeled previously. Figure 16 shows data from F98, IRAS, and MSX along with a smooth model and our canonical clumpy model. We compared the data with our grid of smooth models and confirm that the parameters similar to those given by F98 (they used $r_{in}=0.032\text{pc}$, $r_{out}=2.6\text{pc}$, $\alpha=0.0$, $M=70000M_{\odot}$) produce the best fit, but that fit is still not perfect, in particular shortward of $8\mu\text{m}$ and around $20\mu\text{m}$. We then ran a large number (~ 600) of clumpy models with different clump distributions, inner radii, average radial density gradients, and smooth-to-clumpy ratios (but fixed outer radius), and found the best-fitting sightline by least-squared difference between the data and model. **We fit only the F98 data between 3 and $13\mu\text{m}$, but the best-fitting models also fit the longer wavelength data, with no further adjustment.** In particular, the slope of the SED around $20\mu\text{m}$ and the behavior shortward of $8\mu\text{m}$ resemble the data much more closely than the smooth model. The best-fitting smooth and clumpy models' parameters are listed in Table 2. The figure also shows the SEDs for other sightlines of the same clumpy model as grayscale, showing that if this is indeed an accurate model of G5.89, that it would look rather different from a different vantage point. Figure 17 shows three other objects from F98 with different types of SEDs (NIR intensity and silicate emission or absorption), all of which are fit better by clumpy models than smooth ones (see χ^2 values and models parameters in Table 2). In some cases, the model flux falls short of the observations at longer wavelengths, in particular at $100\mu\text{m}$. At the size of the $100\mu\text{m}$ IRAS beam, the Galaxy is very confused, and nearby sources almost certainly contribute some heating of the outer dust cocoon, increasing the far-IR flux.

Figures 18 and 19 show contours of goodness-of-fit for the smooth and clumpy models, respectively. Smooth models have the same difficulties fitting real data that they did in fitting SEDs from 3-D models above: The better-fitting models have flat density profiles or even ones that increase as a function of radius. The outer radii are uncomfortably large, and

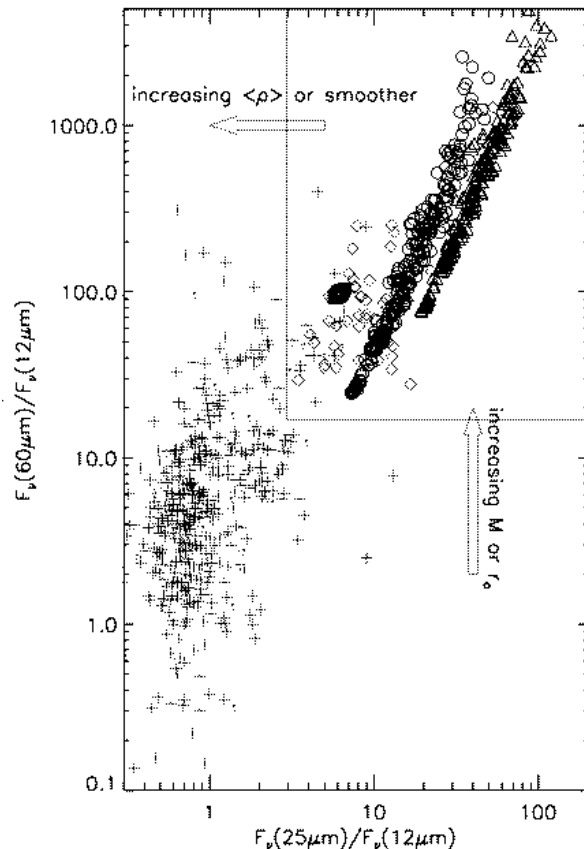


Fig. 15.— IRAS colors of models and real objects in the Galaxy. This color-color diagram is similar to that in WC89, and shows a random sample of field objects (plus signs) along with UHH II regions from Kurtz et al. (1994) and WC89 (diamonds). Colors of a model viewed from different angles are shown for smooth-to-clumpy ratio of 0.03 (triangles), 0.1 (circles), and 0.9 (squares). Our models have the WC89 colors of UCH II models, but so do smooth models – the IRAS bandpasses are not extremely sensitive to dust geometry, although there are clear trends in this color space with the smooth-to-clumpy ratio.

Table 2. Parameters of 1-D and 3-D models fitting data

object	model	density index α	r_i [pc]	r_o [pc]	smooth-to clumpy	mass M_\odot	Average Av to star	χ^2
G5.89-0.39	smooth unconstrained	+1.5	0.00039	0.39	1	1700	109	2.7
	smooth $\alpha \leq 0, r_{out} \leq 7$	0.0	0.0059	5.9	1	2.3×10^5	109	6.1
	clumpy	0.0	0.0001	2.5	0.3	50000	194	2.5
G29.96-0.02	smooth unconstrained	+0.5	0.0039	1.1	1	3500	50	5.8
	smooth $\alpha \leq 0, r_{out} \leq 7$	0.0	0.0039	3.9	1	51000	50	7.1
	clumpy	0.0	0.0001	2.5	0.03	50000	178	1.1
G34.26+0.15	smooth unconstrained	-0.5	0.0039	3.8	1	1.3×10^5	150	11.
	clumpy	-1.0	0.003	2.5	0.1	50000	259	2.5
G75.78+0.34	smooth unconstrained	+0.5	0.0019	19.	1	2.1×10^7	100	4.7
	smooth $\alpha \leq 0, r_{out} \leq 7$	0.0	0.0039	3.9	1	2.0×10^5	200	16.
	clumpy	-0.5	0.0001	2.5	0.3	50000	238	1.7

even the best-fitting models have $\chi^2 \gtrsim 7$.

Clumpy models with a smooth-to-clumpy ratio of $\lesssim 50\%$ are preferred, with a loose preference for the range 0.1–0.3. Models with highly evacuated voids (3% smooth) have more difficulty reproducing the $5\mu\text{m}$ flux and short-wavelength shape of the SED seen in some objects. On the other hand, models too smooth begin to show the shortcomings of the completely smooth models and also fit less well. When considering the radiation intensity in the interior of an externally lit cloud, Bethell et al (2004) found that a smooth-to-clumpy ratio of 0.333 in a hierarchically clumped model produced a similar internal intensity to an externally lit turbulent hydrodynamic simulation – corroborating evidence of a low smooth fraction.

Finally, we note that models with fairly flat angle-averaged radial density profiles often fit better than those with a strong radial gradient, but that the clumpy models with negative gradients (decreasing density with radius) fit better than smooth models with negative gradients. Both findings are important: some UCH II regions such as G5.89 are well-described by a star in a clumpy molecular cloud, without any particularly concentrated envelope. This is consistent with the notion that UCH IIs are relatively evolved protostars, perhaps with accretion already halted (Churchwell 2002). ¹ However, radial density profiles have been invoked to explain the submm spatial intensity distribution of high-mass protostellar objects (e.g. Hatchell et al. 2000). A full analysis of submm radial intensity profiles is beyond the scope of this paper, but preliminary investigation finds that clumpy models with α between -0.5 and -1.0 fit the “non-peaked” SCUBA sources of (Hatchell et al. 2000) as well as 1-D models, and clumpy models with $\alpha \simeq -1.5$ fit the “peaked” sources very well, without needing to invoke extra emission in a “core” as was required by those authors with 1-D models.

In Figure 20, we show something even more remarkable: the single clumpy model that best fits G5.89 can in fact do a reasonable job fitting F98’s entire collection of UCH II regions! We normalized each region’s data to the $100\mu\text{m}$ point, mostly to correct for distance, but this also corrects for the difference in spectral type between the regions. For a deeply embedded object, the shape of the output (observable) SED shows very little variation whether the cocoon is heated by an O7 star or a B2 star, because the NIR/MIR are dominated by reprocessed emission in both cases (see discussion in Whitney et al. 2004b). The total luminosity of the object naturally scales with the bolometric luminosity of the illuminating star. It is very interesting that all of these young protostars are consistent with the same

¹We note that G5.89-0.39 is a multiple source (Feldt et al. 2003; Sollins et al. 2004), which is consistent with our interpretation as an illuminating source embedded in a molecular cloud without any particular radial density gradient. We are currently investigating models with multiple sources, and although beyond the scope of this paper, the SEDs of small clusters show many similar effects to those discussed here.

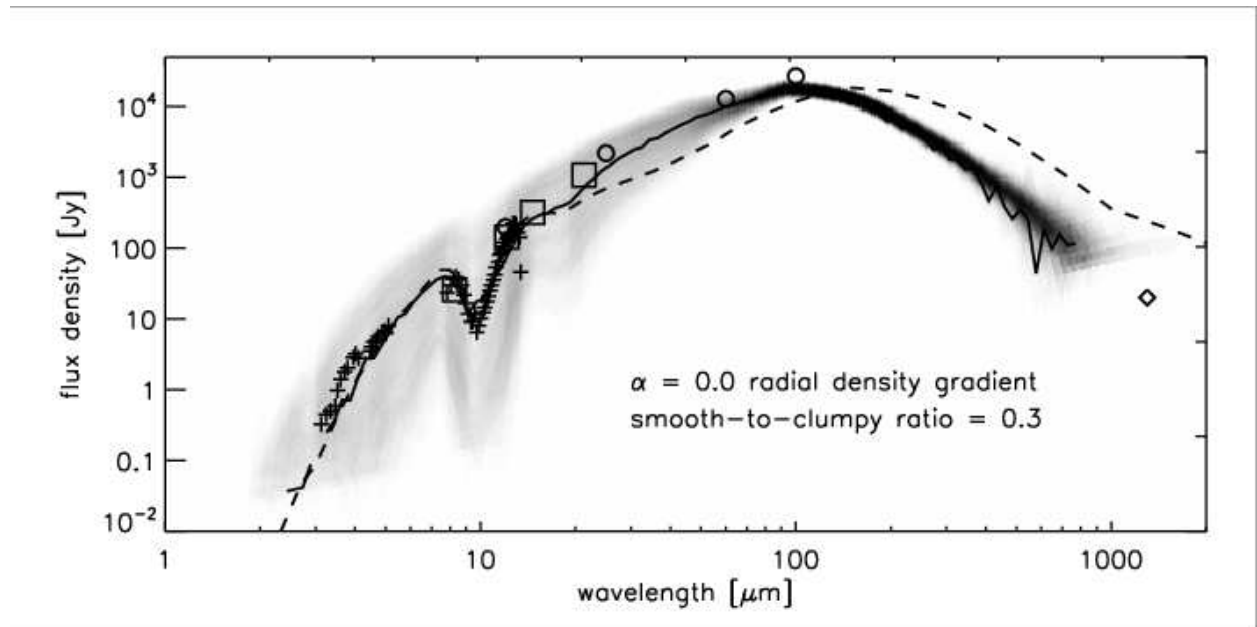


Fig. 16.— Comparison of clumpy models to UCH II region G5.89-0.39. Observations are spectra from F98 (plus signs) and photometry from IRAS (circles), MSX (squares), and Chini et al. (1986) (diamond). The best-fit sightline of a clumpy model is a solid line and the range of SEDs for different sightlines of that same clumpy model (gray scale, darker reflecting a higher density of similar SEDs). Also shown is the best-fitting smooth model (dashed line). The best clumpy sightline fits the data very well; note that we only tried to fit $1 < \lambda < 15 \mu\text{m}$, and that the agreement at longer wavelengths occurred automatically. In particular the clumpy model fits better at 1.3mm datapoint. The clumpy model is constructed with a varying aperture size appropriate to the instruments being shown. This mostly affects the longest and shortest wavelengths.

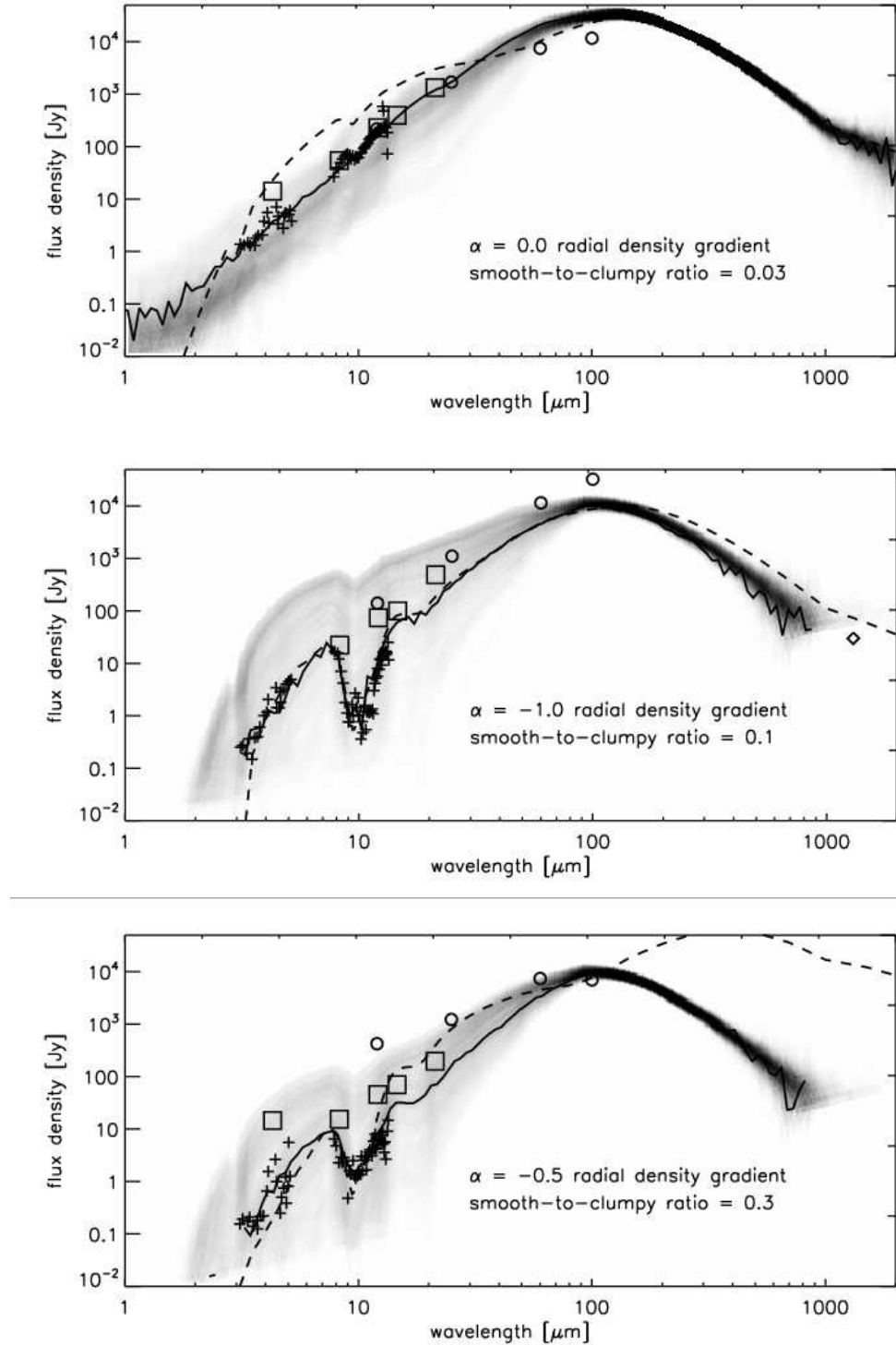


Fig. 17.— Comparison of clumpy models to UCH II regions G29.96-0.02, G34.26+0.15, and G75.78+0.34, annotations as Fig. 16.

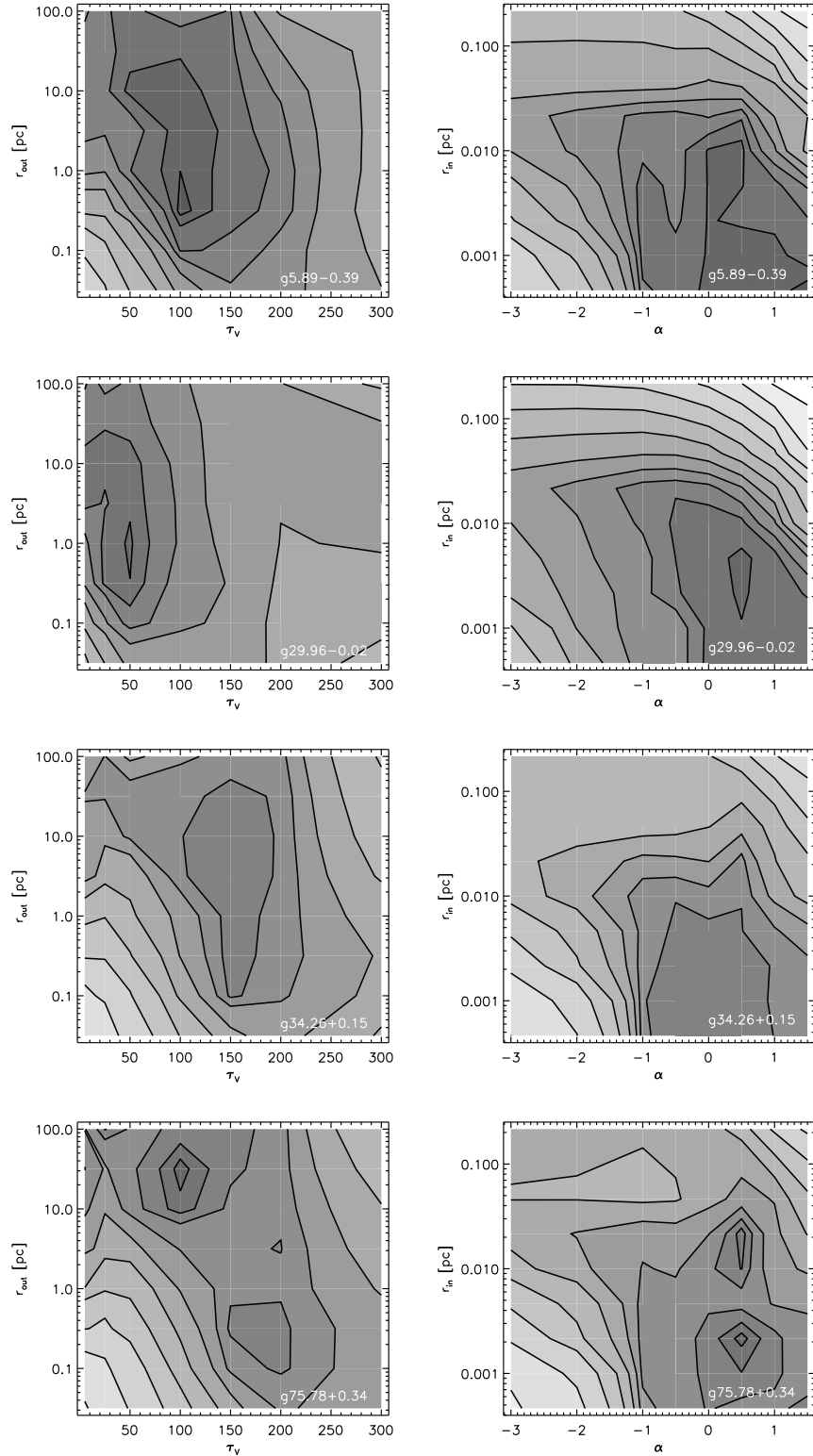


Fig. 18.— Contours of goodness-of-fit of 1-D smooth models to four UCH II regions. The models favor large outer radii and often often large inner radii as well – see text for discussion.

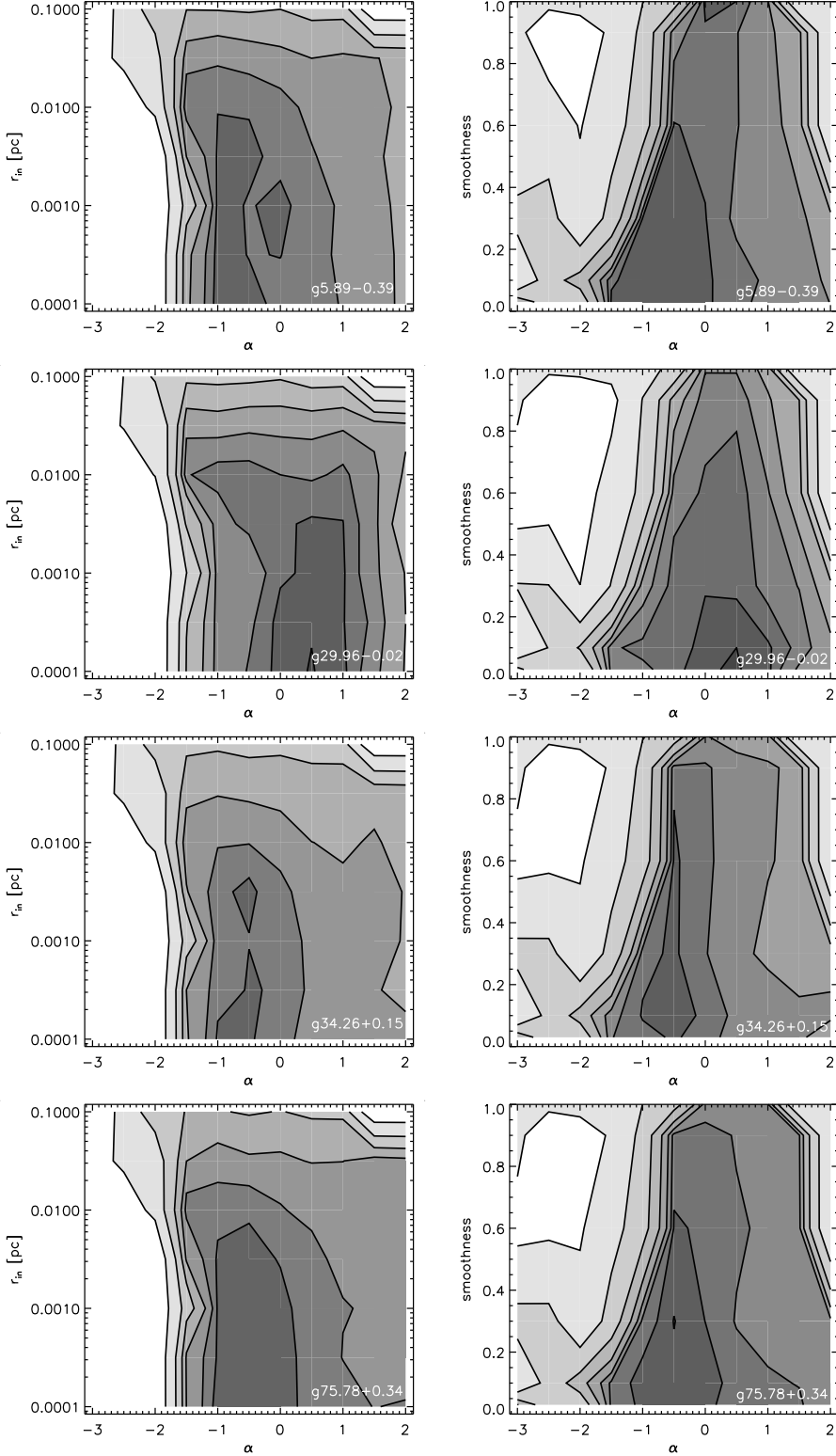


Fig. 19.— Contours of goodness-of-fit of 3-D clumpy models to four UCH II regions. The models favor relatively flat radial profiles and low smooth-to-clumpy ratios, and best fits tend to have lower χ^2 than the best fitting 1-D models – see text for discussion.

model seen from different directions. Observational tests must be done using ensembles of objects, and some care should be taken not to overinterpret differences between individual objects as differences in evolutionary state or cocoon mass.

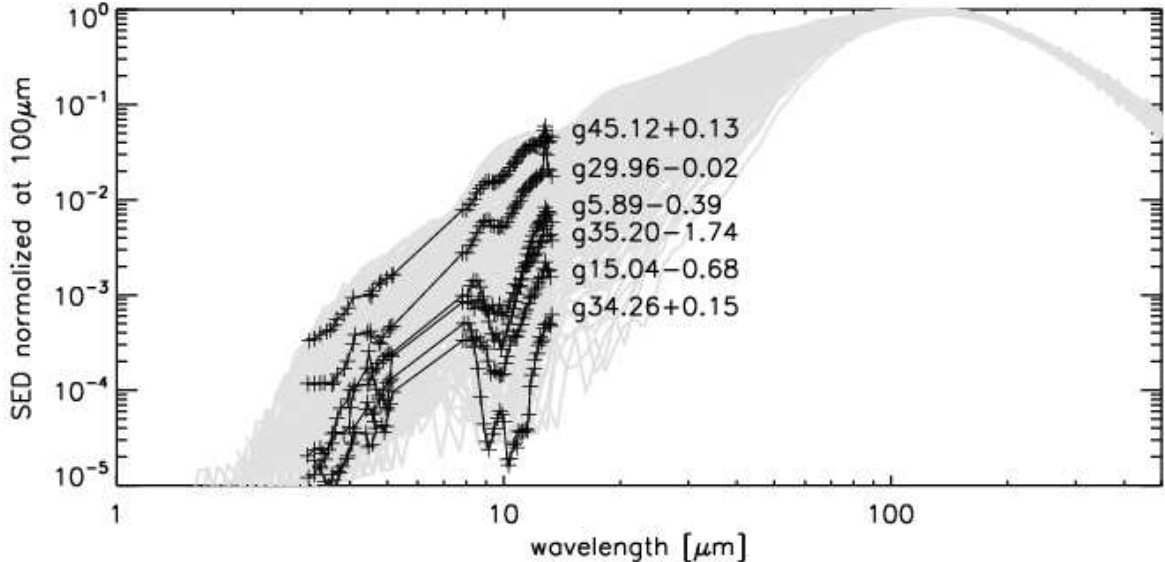


Fig. 20.— The same clumpy model that fits G5.89 (Fig. 16, top panel) can in fact fit F98’s entire sample of UCH II regions reasonably well! Data for several regions are here plotted as connected plus signs on top of the gray-scale range of sightlines for a single clumpy model.

6. Conclusions

We use 3-D radiative transfer models to examine the importance of an inhomogeneous circumstellar envelope on the observed properties of young embedded massive stars. The spectral energy distributions of 3-D models vary significantly with viewing angle, and differ significantly from 1-D models. Some of our most important findings are as follows:

- The SEDs of embedded stars and young stellar objects are significantly affected by clumping of the dust at wavelengths $\lesssim 100\mu\text{m}$. Longer-wavelength emission is primarily determined by the total mass of thermally emitting dust rather than its distribution, and therefore less affected by clumping.
- Silicate features (the strongest and most noticeable at $10\mu\text{m}$) can be seen in emission or absorption in *same object*, depending on viewing angle.

- Attempts to fit 3-D clumpy objects with 1-D models can mis-estimate the size of the region and total mass by more than an order of magnitude. The derived values of the region size, mass, central object luminosity, and optical depth are very often incorrect by a factor of 2–3.
- The typical or average SED (considering all viewing angles) is sensitive to the overall smoothness of the dust distribution, or the smooth-to-clumpy ratio. The UCH IIs observed by F98 are best fit by models that are $\lesssim 50\%$ smooth.
- Our 3-D models do a better job at fitting the entire SED of UCH IIs than previous 1-D models, and can easily explain the variation in UCH II SEDs as differences in viewing angle of a clumpy medium.
- Using 3-D clumpy models tends to allow the data to be fit well with more peaked density profiles than the best 1-D fits, which may agree better with SCUBA imaging data. Some UCH II are best fit with flat density profiles, whether one uses 1-D or 3-D models – these may be more evolved objects best understood as just a hot star embedded in a non-accreting cloud.

It is becoming clear that models with more than one dimension are necessary to understand the observed properties of interstellar and circumstellar dust and gas. We have shown here that clumpiness can severely affect the emergent spectral energy distribution of embedded massive stars and UCH II regions. Previous work by us and others has shown that at least two-dimensional models are critical to understanding accreting protostars; clumpiness in such YSOs may have further effects. In the general ISM, clumpiness affects the radial profiles and line ratios observed in H II regions Wood et al. (2005). Clumping has been invoked to explain the observed silicate feature in AGN torii Nenkova, Ivezić, & Elitzur (2005). Models such as our code are invaluable to determine which physical parameters are observationally accessible in complex and multi-phase systems.

Acknowledgements

During this work, RI was supported by the GLIMPSE *Spitzer* Legacy program (E Churchwell, P.I.), BW by NASA LTSA (NAG5-8933), and KJ an NSF AST postdoctoral fellowship. This publication used data from 2MASS, MSX, and IRAS, and made extensive use of NASA’s ADS abstract service. The Two Micron All Sky Survey is a joint project of the University of Massachusetts and IPAC/Caltech, funded by NASA and NSF. Processing

of Midcourse Space Experiment Data was funded by the Ballistic Missile Defense Organization with additional support from NASA. The data are served by the NASA/IPA Infrared Science Archive operated by JPL/Caltech.

We thank Ed Churchwell, John Mathis, and Jon Bjorkman for useful discussions on massive star formation, interstellar clumps, and radiative transfer.

REFERENCES

Allen, L. E., et al. 2004, *ApJS*, 154, 363
Benjamin, R. A., et al. 2003, *PASP*, 115, 953
Bethell, T. J., Zweibel, E. G., Heitsch, F., & Mathis, J. S. 2004, *ApJ*, 610, 801.
Beuther, H., Schilke, P., Menten, K. M., Motte, F., Sridharan, T. K., & Wyrowski, F. 2002, *ApJ*, 566, 945
Bjorkman, J. E. & Wood, K. 2001, *ApJ*, 554, 615
Chini, R., Kreysa, E., Mezger, P. G., & Gemuend, H.-P. 1986, *A&A*, 154, L8
Churchwell, E. 2002, *ARA&A*, 40, 27
Churchwell, E. et al. 2004, *ApJS*, 154, 322
Elmegreen, B. G. 1997, *ApJ*, 477, 196
Elmegreen, B. G., & Falgarone, E. 1996, *ApJ*, 471, 816
Faison, M., Churchwell, E., Hofner, P., Hackwell, J., Lynch, D. K., & Russell, R. W. 1998, *ApJ*, 500, 280 (F98)
Fazio, G. G. et al. 2004, *ApJS*, 154, 10
Feldt, M., et al. 2003, *ApJ*, 599, L91
Hatchell, J., Fuller, G. A., Millar, T. J., Thompson, M. A., & Macdonald, G. H. 2000, *A&A*, 357, 637
Ivezic, Z. & Elitzur, M. 1997, *MNRAS*, 287, 799
Kim, S., Martin, P. G., & Hendry, P. D. 1994, *ApJ*, 422, 164
Kurtz, S., Churchwell, E., & Wood, D. O. S. 1994, *ApJS*, 91, 659
Laor, A., & Draine, B. T. 1993, *ApJ*, 402, 441
Mathis, J. S., Whitney, B. A., & Wood, K. 2002, *ApJ*, 574, 812
Megeath, S. T., et al. 2004, *ApJS*, 154, 367
Misselt, K. A., Gordon, K. D., Clayton, G. C., & Wolff, M. J. 2001, *ApJ*, 551, 277
Mueller, K. E., Shirley, Y. L., Evans, N. J., & Jacobson, H. R. 2002, *ApJS*, 143, 469
Nenkova, M., Ivezic, Z., Elitzur, M. 2005 *ApJ*, submitted.
Reach, W. T. et al. 2004, *ApJS*, 154, 385
Rieke, G. H. et al. 2004, *ApJS*, 154, 25
Sollins, P. K., et al. 2004, *ApJ*, 616, L35

van der Tak, F. F. S., van Dishoeck, E. F., Evans, N. J., & Blake, G. A. 2000, *ApJ*, 537, 283
Whitney, B. A., Wood, K., Bjorkman, J. E., & Wolff, M. J. 2003a, *ApJ*, 591, 1049 (Paper I)
Whitney, B. A., Wood, K., Bjorkman, J. E., & Cohen, M. 2003b, *ApJ*, 598, 1099 (Paper II)
Whitney, B. A. et al. 2004a, *ApJS*, 154, 315
Whitney, B. A., Indebetouw, R., Bjorkman, J. E., & Wood, K. 2004b, *ApJ*, 617, 1177 (Paper III)
Wolf, S., Fischer, O., & Pfau, W. 1998, *A&A*, 340, 103
Wolfire, M. G., & Churchwell, E. 1994, *ApJ*, 427, 889
Wood, D. O. S., & Churchwell, E. 1989, *ApJ*, 340, 265
Wood, K., Haffner, L. M., Reynolds, R. J., Mathis, J. S., & Madsen, G. 2005, *ApJ* submitted.